Although the timing of Monsoon Termination II is consistent with Northern Hemisphere insolation forcing, not all evidence of climate change at about this time is consistent with such a mechanism (Fig. 3). Sea level apparently rose to levels as high as –21 m as early as 135 ky before the present (*27*, *28*), preceding most of the insolation rise. The half-height of marine oxygen isotope Termination II has been dated at 135 ± 2.5 ky (*29*). Speleothem evidence from the Alps indicates temperatures near present values at 135 ± 1.2 ky (*31*). The half-height of the $\delta^{18}O$ rise at Devils Hole (142 ± 3 ky) also precedes most of the insolation rise (*20*). Increases in Antarctic temperature and atmospheric CO_2 (*32*) at about the time of Termination II appear to have started at times ranging from a few to several millennia before most of the insolation rise (*4*, *32*, *33*). On the other hand, Monsoon Termination II coincides within error with the final rise in sea level to full Last Interglacial values (*6*, *21–23*, *28*, *34*, *35*) and the last rise to full Last Interglacial $\delta^{18}O$ at Soreq Cave (*12*) and Crevice Cave (*36*). Thus, Monsoon Termination II appears to be an event forced by Northern Hemisphere insolation change, coincident with other such events but after a number of events not directly caused by Northern Hemisphere orbital forcing. As such, it may mark the inception of full interglacial conditions worldwide.

References and Notes

1. W. Dansgaard *et al.*, *Nature* **364**, 218 (1993).
2. The Greenland Summit Ice Cores CD-ROM (1997). Available from the National Snow and Ice Data Center, University of Colorado at Boulder, and the World Data Center-A for Paleoclimatology, National Geophysical Data Center, Boulder, CO. Also available online at www.ngdc.noaa.gov/paleo/icecore/greenland/summit/document/gispisot.htm.
3. Y. J. Wang *et al.*, *Science* **294**, 2345 (2001).
4. W. S. Broecker, G. M. Henderson, *Palaeoceanography* **13**, 352 (1998).
5. Oxygen isotope analyses were performed at the Isotope Laboratory, Institute of Karst Geology, Guilin, China, using a VG MM-903 gas mass spectrometer (for Dongge Cave D3 and D4 analyses, except for D4 between 15.81 ky and 9.98 ky); at the State Key Laboratory of Loess and Quaternary Geology, Institute of Earth Environment, Xi'an, China, using a Finnigan MAT 252 Kiel Device III (Dongge Cave D4 between 15.81 and 9.98 ky); and on a Finnigan MAT 251 at the Nanjing Institute of Geology and Paleontology, Chinese Academy of Sciences (Hulu Cave H82 between 15.34 and 16.30 ky before the present). Other H82 analyses were reported earlier in (*3*).
6. R. L. Edwards, J. H. Chen, G. J. Wasserburg, *Earth Planet. Sci. Lett.* **81**, 175 (1987).
7. H. Cheng *et al.*, *Chem. Geol.* **169**, 17 (2000).
8. C.-C. Shen *et al.*, *Chem. Geol.* **185**, 165 (2002).
9. C. H. Hendy, *Geochim. Cosmochim. Acta* **35**, 801 (1971).
10. In detail, D3 and D4 do not replicate perfectly, with some times characterized by differences in $\delta^{18}O$ that are large as compared to analytical error but small compared to the amplitude of the record (Fig. 2). These discrepancies are likely due to kinetic effects, water/rock interactions, and/or differential evaporation of water at the land surface. There is little evidence for kinetic fractionation on the basis of C and O isotope correlations. C and O isotope ratios do not correlate strongly for any of the three stalagmites in this study or even for portions of these stalagmites. The highest R^2 value for any of the three stalagmites is 0.27 (table S6). Because the top of D4 was deposited in isotopic equilibrium and because a portion of D4 replicates the Hulu record, D4 is less likely to have been affected by kinetic effects or water/rock interactions than D3.
11. I. Friedman, J. R. O'Neil, *U.S. Geol. Surv. Prof. Pap. 440-KK* (1977).
12. M. Bar-Matthews *et al.*, *Geochim. Cosmochim. Acta* **67**, 3181 (2003).
13. D. Fleitmann *et al.*, *Science* **300**, 1737 (2003).
14. R. Gomez, L. Gonzalez, H. Cheng, R. L. Edwards, F. Urbani, *Geol. Soc. Am. Abstr. Programs* **35**, 587 (2003).
15. W. Dansgaard, *Tellus* **16**, 436 (1964).
16. We used the following form of the Rayleigh equation, modified from (*37*): $(1000 + \delta_p)/(1000 + \delta_{sw}) = f^{(\alpha - 1)}$, where δ_p is the $\delta^{18}O$ of meteoric precipitation, δ_{sw} is the $\delta^{18}O$ of seawater, f is the fraction of the original water vapor remaining, and α is the water/vapor fractionation factor. We assumed a constant α of 1.0094. We used the following values in our calculations: (i) Mid-Holocene/Last Interglacial values: calcite $\delta^{18}O_{VPDB} = -9.2‰$, temperature 1°C > today, and seawater $\delta^{18}O_{SMOW} = 0.0‰$. (ii) Today: calcite $\delta^{18}O_{VPDB} = -8.1‰$ and seawater $\delta^{18}O_{SMOW} = 0.0‰$. (iii) Glacial times: calcite $\delta^{18}O_{VPDB} = -4.5‰$ and temperature 4°C. (VPDB, Vienna Pee Dee belemnite standard.)
17. M. A. Maslin, S. J. Burns, *Science* **290**, 2285 (2000).
18. J. Jouzel, G. Hoffmann, R. D. Koster, V. Masson, *Quat. Sci. Rev.* **19**, 363 (2000).
19. C. D. Charles, D. Rind, J. Jouzel, R. D. Koster, R. G. Fairbanks, *Science* **263**, 508 (1994).
20. I. J. Winograd *et al.*, *Quat. Res* **48**, 141 (1997).
21. J. H. Chen, H. A. Curran, B. White, G. J. Wasserburg, *Geol. Soc. Am. Bull.* **103**, 82 (1991).
22. C. H. Stirling, T. M. Esat, K. Lambeck, M. T. McCulloch, *Earth Planet. Sci. Lett.* **160**, 745 (1998).
23. D. R. Muhs, K. R. Simmons, B. Steinke, *Quat. Sci. Rev* **21**, 1355 (2002).
24. A. Berger, *J. Atmos. Sci.* **35**, 2362 (1978).
25. J. E. Kutzbach, *Science* **214**, 59 (1981).
26. Z.-S. An, S. Porter, *Geology* **25**, 603 (1995).
27. M. Stein *et al.*, *Geochim. Cosmochim. Acta* **57**, 2541 (1993).
28. C. D. Gallup, H. Cheng, F. W. Taylor, R. L. Edwards, *Science* **295**, 310 (2002).
29. G. Henderson, N. Slowey, *Nature* **404**, 61 (2000).
30. R. G. Fairbanks, *Nature* **342**, 637 (1989).
31. C. Spotl, A. Mangini, N. Frank, R. Eichstadter, S. J. Burns, *Geology* **30**, 815 (2002).
32. J. R. Petit, *Nature* **399**, 429 (1999).
33. M. Bender, T. Sowers, L. Labeyrie, *Global Biogeochem. Cyc.* **8**, 363 (1994).
34. R. L. Edwards, C. D. Gallup, K. B. Cutler, H. Cheng, in *Treatise on Geochemistry, Volume 6: The Oceans and Marine Geochemistry*, H. Elderfield, Ed. (Elsevier, Oxford, 2004), pp. 343–364.
35. N. C. Slowey, G. M. Henderson, V. B. Curry, *Nature* **383**, 242 (1996).
36. J. A. Dorale, thesis, University of Minnesota, Twin Cities, MN (2000).
37. R. E. Criss, *Principles of Stable Isotope Distribution* (Oxford Univ. Press, New York, 1999), p. 108.

38. We especially thank G. Comer and W. S. Broecker for their tremendous and generous support of our work. We thank H. Wang, Y. Fong, and L. Tu for stable isotope analyses and Y. Xie, S. He, J. Cao, Z. Wang, J. Zhan, and D. Yu for assistance with fieldwork. Supported by NSF grants ESH0214041, ESH9809459, and MRI0116395; a Comer Science and Education Foundation Grant (CC8); National Science Foundation of China grants 40328005 and 40231008; and grants from the Ministry of Land and Resources and the Ministry of Science and Technology of China.

Supporting Online Material

www.sciencemag.org/cgi/content/full/304/5670/575/DC1

Tables S1 to S6

References

8 September 2003; accepted 24 March 2004

Early Life Recorded in Archean Pillow Lavas

Harald Furnes,[1]*† Neil R. Banerjee,[1,2]† Karlis Muehlenbachs,[2] Hubert Staudigel,[3] Maarten de Wit[4]

Pillow lava rims from the Mesoarchean Barberton Greenstone Belt in South Africa contain micrometer-scale mineralized tubes that provide evidence of submarine microbial activity during the early history of Earth. The tubes formed during microbial etching of glass along fractures, as seen in pillow lavas from recent oceanic crust. The margins of the tubes contain organic carbon, and many of the pillow rims exhibit isotopically light bulk-rock carbonate $\delta^{13}C$ values, supporting their biogenic origin. Overlapping metamorphic and magmatic dates from the pillow lavas suggest that microbial life colonized these subaqueous volcanic rocks soon after their eruption almost 3.5 billion years ago.

Biologically mediated corrosion of synthetic glass is a well-known phenomenon (*1*). Early studies of natural volcanic glass suggested that colonizing microbes can actively dissolve glass substrates to extract nutrients, thereby producing channel-like tubular structures (*2*, *3*). This mechanism has been verified experimentally (*4–7*). Over the past decade, numerous studies have documented micrometer-sized corrosion structures produced by microbial activity in natural basaltic glasses throughout the upper few hundreds of meters of the oceanic crust (*8–13*). These structures have textural characteristics (such as size range, morphology, and organization) that are consistent with a biogenic origin. The presence of carbon and nitrogen (*10*, *12*, *13*) as well as nucleic acids associated with the corrosion textures (*10*, *13*) and characteristically depleted $\delta^{13}C$ values of disseminated carbonate within microbially altered basaltic glass (*10*, *13*, *14*) further support the biogenic origin of these structures. In this paper, we document evidence of ancient microbial activity within exceptionally well-preserved pillow lavas of the ~3.5 billion-year-old Bar-

berton Greenstone Belt (BGB), South Africa (Fig. 1).

The BGB comprises 5 to 6 km of predominantly komatiitic and basaltic pillow lavas and sheet flows and related intrusions that are interlayered with cherts and overlain by cherts, banded iron formations, and shales (*15*). This magmatic sequence has been interpreted to represent 3480- to 3220-million-year-old oceanic crust and island arc assemblages (*16*). These rocks have undergone metamorphism from prehnite-pumpellyite to greenschist facies (*15*, *17*).

Within the originally glassy rims of many BGB pillow lavas, dense populations of mineralized tubular structures 1 to 9 μm in width (average width, 4 μm) and up to 200 μm in length (average length, ~50 μm) are observed (Fig. 1, D and E). These structures consist of fine-grained titanite and extend away from healed fractures along which seawater once flowed (Fig. 1C). Some of these tubular structures exhibit segmentation into subspherical bodies approximately 1 to 9 μm in diameter (Fig. 1, E and F). In some cases, chlorite has overgrown these structures at the segmentation sites (Fig. 1F). These tubular structures are similar in size, shape, and distribution to features documented in glassy pillow rims from the Troodos ophiolite (Fig. 2, A and B) and recent oceanic crust (Fig. 2, C and D). The structures shown in Fig. 1, D to F, are interpreted as being the mineralized remains of microbial borings in previously glassy rocks (Fig. 2). Tubular structures such as those shown in Fig. 2 have not been successfully replicated by abiotic glass-dissolution experiments (*4*–*7*).

X-ray element mapping (*18*) demonstrates the presence of carbon along the walls of the tubular structures (Fig. 3). The calcium, iron, and magnesium maps of the same region all show anticorrelation with carbon, indicating that the carbon is not bound in carbonate (Fig. 3). Biofilms and organic remains containing nucleic acids are commonly observed along the interior surface of microbially generated channels in volcanic glass from recent oceanic crust (*8*, *10*, *12*–*14*). The carbon is therefore interpreted to represent organic material left behind along the interior surface of the microbially generated tubes that was subsequently preserved during later mineralization by titanite.

Disseminated carbonate from bulk rock subsamples (*19*) of the formerly glassy rims have $\delta^{13}C$ values of +3.9 to –16.4 per mil (‰), which are different from those of the crystalline interiors of individual pillows [+0.7 to –6.9‰ (Fig. 4A)]. Secondary carbonate-rich amygdules have $\delta^{13}C$ values that cluster around zero. The $\delta^{13}C$ values from crystalline interior samples are bracketed between those of primary mantle CO_2 (–5 to –7‰) and of Archean marine carbonate (0‰) (*20*), whereas the glassy samples extend to lower $\delta^{13}C$ values. Such isotopic contrasts are also seen in pillow lava rims from ophiolites (Fig. 4B) and oceanic crust (Fig. 4C), where the generally low $\delta^{13}C$ values of disseminated carbonate are attributed to metabolic byproducts formed during microbial oxidation of dissolved organic matter in pore waters (*13*, *14*, *21*). The isotopically low $\delta^{13}C$ values of carbonate in the formerly glassy rims of the BGB pillows are thus interpreted to have also formed by microbial fractionation.

In order to determine the timing of the microbial activity, we must document the relationships between the tubular structures and metamorphic mineral growth. Step-heating $^{40}Ar/^{39}Ar$ analyses of amphiboles from serpentinized komatiitic basalts within the Komati Formation of the BGB give a metamorphic age of 3486 ± 8 million years ago (Ma) (*22*). This $^{40}Ar/^{39}Ar$ age overlaps U/Pb dates of magmatic zircons from the same outcrops (3482 Ma) and cherts directly overlying the pillow lavas (3472 ± 2 Ma) (*16*, *22*–*24*). The similarity of these ages and the preservation of igneous spinifex textures pseudomorphed by metamorphic minerals suggest that

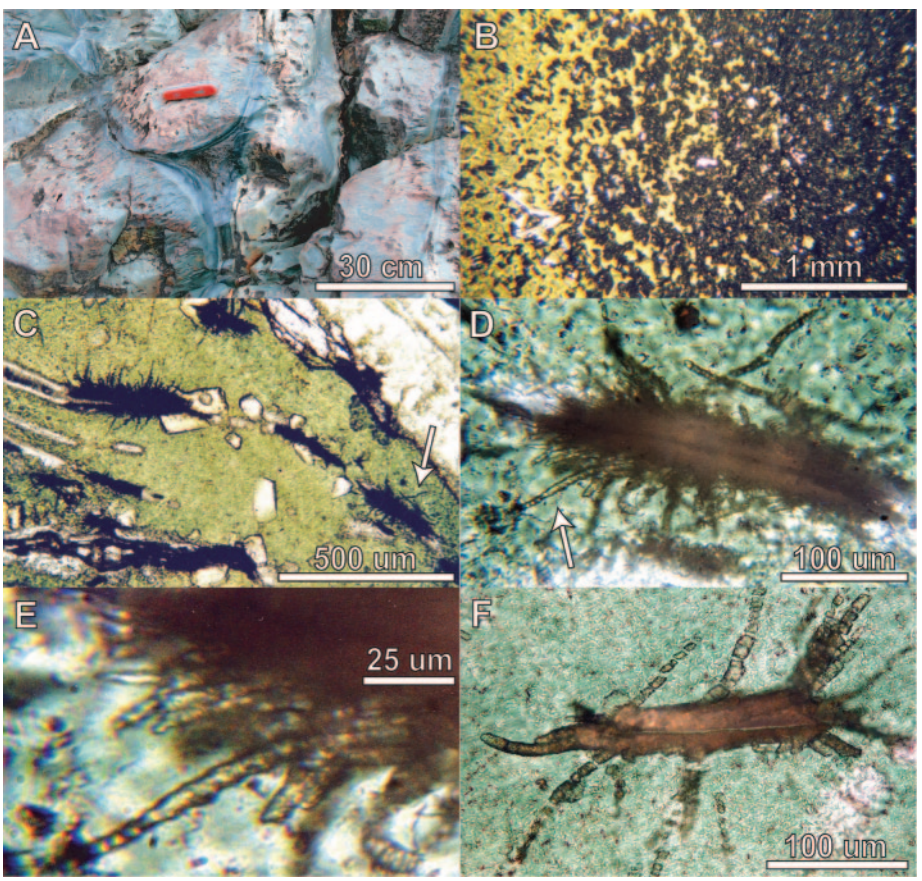

Fig. 1. Pillow lavas and microbial textures in pillow lavas from the Hooggenoeg and Kromberg Formations of the Onverwacht Group, BGB. (**A**) Well-preserved pillow lava from the Kromberg Formation. The size of pillows is highly variable (ranging from centimeters to ~2 m across), and they are non- to moderately amygdaloidal, indicating eruption in deep to shallow water, respectively. The originally chilled glassy rims are marked by a dark zone 1 to 2 cm thick. (**B**) Photomicrograph of a pillow rim (sample 40-BG-03) from the lower part of the Kromberg Formation. The outermost chilled zone (yellow) consists of altered glass enclosing small (50 to 100 μm) isolated varioles. Varioles increase in size, and they begin to coalesce inward until the pillow is holocrystalline about 2 cm from the outer margin. (**C**) Photomicrograph of pillow rim (sample 29-BG-03) from the uppermost part of the Hooggenoeg Formation. The original glass (replaced by chlorite) exhibits healed fractures along which numerous microbially generated tubular structures mineralized by titanite are rooted. (**D**) Detail of (C) [indicated by arrow in (C)] showing well-developed microbially generated tubular structures [arrow shows a blown-up part of (D)]. (**E**) Detail from left part of (D). Note the segmented character of some of the tubes (lower left). (**F**) Photomicrograph (sample 29-BG-03) of chlorite overprinting the microbially generated tubular structures.

[1]Department of Earth Science, University of Bergen, Allegaten 41, 5007 Bergen, Norway. [2]Department of Earth and Atmospheric Sciences, University of Alberta, Edmonton, Alberta T6G 2E3, Canada. [3]Scripps Institution of Oceanography, University of California, La Jolla, CA 92093–0225, USA. [4]Centre for Interactive Graphical Computing of Earth Systems, Geological Sciences, University of Cape Town, Rondebosch 7701, South Africa.

*To whom correspondence should be addressed. E-mail: Harald.Furnes@geo.uib.no
†These authors contributed equally to this work.

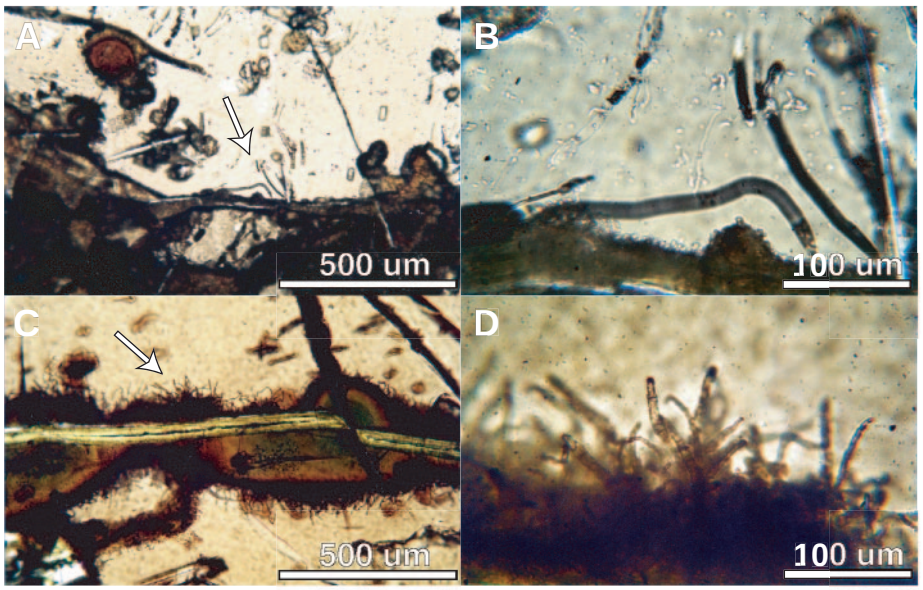

Fig. 2. Tubular structures of inferred microbial origin in basaltic glass from the Troodos ophiolite (**A** and **B**) and modern oceanic crust (**C** and **D**). (A) Photomicrograph of the glassy chilled margin of a pillow (sample CY-1-35). (B) Detail from (A) [indicated by arrow in (A)] showing tubular structures in fresh glass. (C) Photomicrograph of a modern pillow margin (Ocean Drilling Program sample 148-896A, 11R-01, 73-75 cm) showing microbial alteration features of fresh basaltic glass (light yellow) along fractures. (D) Detail from (C) [indicated by arrow in (C)] showing tubular structures of microbial origin protruding into the fresh glass.

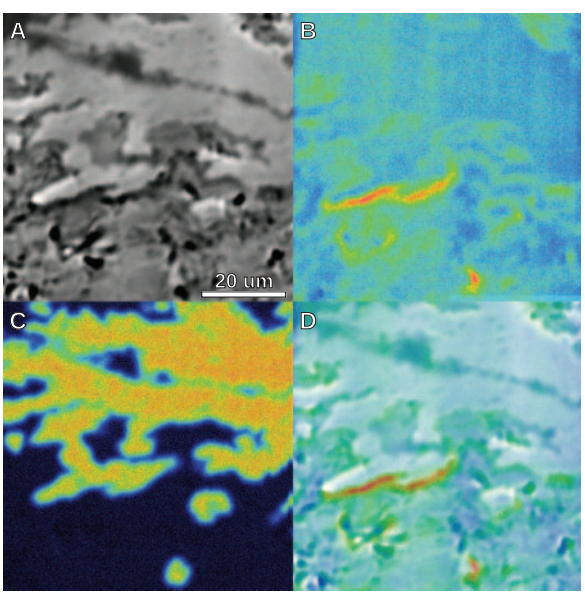

Fig. 3. Backscatter electron (BSE) image (**A**) and x-ray element maps of carbon (**B**) and calcium (**C**) associated with tubular structures from approximately the same area shown in Fig. 1E. In (**D**), the carbon map has been superimposed on the BSE image, showing the association of carbon with the margins of the tubular features. An x-ray element map of titanium is shown in fig. S1.

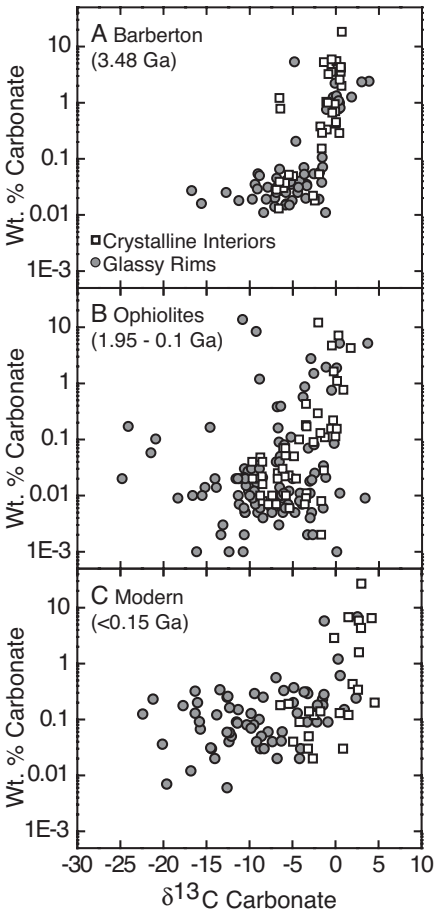

Fig. 4. Relationship between weight % carbonate versus $\delta^{13}C$ for the originally glassy rims (solid circles) and crystalline interiors (open squares) of pillows. (**A**) Analyses from pillow lavas of the Komati, Hooggenoeg, and Kromberg Formations of the Onverwacht Group, BGB. (**B**) Compilation of analyses from the Troodos ophiolite, Cyprus; the Mirdita ophiolite, Albania; the Solund-Stavfjord ophiolite, Norway; and the Jormua ophiolite, Finland (*21*). (**C**) Compilation of analyses from modern oceanic crust (*13*, *14*). Ga, billion years ago.

the metamorphic overprint occurred penecontemporaneously with igneous activity (*15*, *23*). Oxygen isotope and metamorphic profiles across the BGB magmatic stratigraphy are indistinguishable from those of Phanerozoic ophiolites and recent oceanic crust (*25*, *26*). This implies that the metamorphism represents ancient ocean floor hydrothermal alteration.

The morphology of the delicate structures illustrated in Fig. 1, C to F, is inconsistent with inorganic precipitation of titanite during seafloor metamorphism of the BGB pillow lavas. Fine-grained chlorite is observed to have overgrown the titaniferous tubular structures, which in some cases caused segmentation (Fig. 1F). These observations imply that the delicate tubular structures existed before the precipitation of titanite and chlorite and are thus premetamorphic (Fig. 1, C to F). The lack of later regional metamorphic events that may have caused recrystallization has allowed preservation of this 3.48 billion-year-old biomarker.

Our data come from a geological setting that has not been extensively explored in the search for early life on Earth. The suggestion of volcanic rocks from the oceanic crust as a habitat for early microbial life and the preservation of associated biomarkers is not unexpected. Some of the deepest branches in the tree of life are populated by thermophilic microbes, and there is increasing evidence that early life may have been connected to volcanic environments, such as deep-sea hydrothermal vents (*27*). This is consistent with an optimal growth temperature for thermophilic microbes of 70°C, determined from the only study to investigate the depth distribution of microbial alteration textures in the modern oceans (*11*). Filamentous microfossils have been described from a 3235 million-year-old massive sulfide deposit interpreted to have formed in much the same way as modern black smokers (*28*). Our study indicates that microbes colonized basaltic glass of the early oceanic crust, much in the same way as they do modern volcanic glass. Well-preserved pillow lavas, which are a major component of Archean greenstone

belts, may thus be one of the most promising places to search for vestiges of early life on Earth.

References and Notes

1. W. E. Krumbein, C. A. Urzi, C. Gehrman, *Geomicrobiol. J.* **9**, 139 (1991).
2. K. A. Ross, R. V. Fisher, *Geology* **14**, 571 (1986).
3. I. H. Thorseth, H. Furnes, M. Heldal, *Geochim. Cosmochim. Acta* **56**, 845 (1992).
4. I. H. Thorseth, H. Furnes, O. Tumyr, *Chem. Geol.* **119**, 139 (1995).
5. H. Staudigel, R. A. Chastain, A. Yayanos, W. Bourcier, *Chem. Geol.* **126**, 147 (1995).
6. H. Staudigel *et al.*, *Earth Planet. Sci. Lett.* **164**, 233 (1998).
7. J. R. Rogers, P. C. Bennett, *Chem. Geol.* **203**, 91 (2004).
8. I. H. Thorseth, T. Torsvik, H. Furnes, K. Muehlenbachs, *Chem. Geol.* **126**, 137 (1995).
9. M. R. Fisk, S. J. Giovannoni, I. H. Thorseth, *Science* **281**, 978 (1998).
10. T. Torsvik, H. Furnes, K. Muehlenbachs, I. H. Thorseth, O. Tumyr, *Earth Planet. Sci. Lett.* **162**, 165 (1998).
11. H. Furnes, H. Staudigel, *Earth Planet. Sci. Lett.* **166**, 97 (1999).
12. H. Furnes *et al.*, *Geochem. Geophys. Geosyst.* **2**, 2000GC000150 (2001).
13. N. R. Banerjee, K. Muehlenbachs, *Geochem. Geophys. Geosyst.* **4**, 2002GC000470 (2003).
14. H. Furnes, K. Muehlenbachs, T. Torsvik, I. H. Thorseth, O. Tumyr, *Chem. Geol.* **173**, 313 (2001).
15. M. J. de Wit, R. A. Hart, J. Hart, *J. Afr. Earth Sci.* **6**, 681 (1987).
16. C. E. J. de Ronde, M. J. De Wit, *Tectonics* **13**, 983 (1994).
17. M. M. Tice, B. C. Bostick, D. R. Lowe, *Geology* **32**, 37 (2004).
18. The x-ray mapping was carried out using a JEOL JXA-8900R microprobe, with an accelerating voltage of 15 kV and probe current of 3×10^{-8} on an iridium-coated thin section.
19. Carbon stable-isotope analyses of disseminated carbonates in glassy and crystalline whole rocks were performed by pouring 100% phosphoric acid onto rock powders under vacuum and analyzing the exsolved CO_2 on a Finnigan MAT 252 mass spectrometer (*14*). The data are reported in the usual delta notation with respect to the Vienna Pee Dee belemnite standard.
20. K. Nakamura, Y. Kato, *Geochim. Cosmochim. Acta* **67** (suppl. 1), A326 (2003).
21. H. Furnes, K. Muehlenbachs, in *Ophiolites in Earth's History*, Y. Dilek, P. T. Robinson, Eds. (Special Publication 218, Geological Society of London, London, 2003), pp. 415–426.
22. M. Lopez- Martinez, D. York, J. A. Hanes, *Precambrian Res.* **57**, 91 (1992).
23. S. L. Kamo, D. W. Davis, *Tectonics* **13**, 167 (1994).
24. J. Dann, *S. Afr. J. Geol.* **103**, 47 (2000).
25. S. E. Hoffman, M. Wilson, D. S. Stakes, *Nature* **321**, 55 (1986).
26. M. J. de Wit, R. A. Hart, *Lithos* **30**, 309 (1993).
27. M. J. Russel, A. J. Hall, *J. Geol. Soc. London* **154**, 377 (1997).
28. B. Rasmussen, *Nature* **405**, 676 (2000).

29. Comments by A. Lepland, B. Robins, T. Chacko, and three anonymous reviewers improved the manuscript. We thank O. Levner for help with carbon isotope analyses and S. Matveev for help with the electron microprobe. Thanks to F. Daniels for hospitality and the Mpumalanga Parks Board for access during field work. Financial support to carry out this study was provided by the Norwegian Research Council, the National Sciences and Engineering Research Council of Canada, the U.S. National Science Foundation, the Agouron Institute, and the National Research Foundation of South Africa.

Supporting Online Material

www.sciencemag.org/cgi/content/full/304/5670/578/DC1
Fig. S1

21 January 2004; accepted 22 March 2004

The Fine-Scale Structure of Recombination Rate Variation in the Human Genome

Gilean A. T. McVean,[1]*† Simon R. Myers,[1]* Sarah Hunt,[2] Panos Deloukas,[2] David R. Bentley,[2] Peter Donnelly[1]

The nature and scale of recombination rate variation are largely unknown for most species. In humans, pedigree analysis has documented variation at the chromosomal level, and sperm studies have identified specific hotspots in which crossing-over events cluster. To address whether this picture is representative of the genome as a whole, we have developed and validated a method for estimating recombination rates from patterns of genetic variation. From extensive single-nucleotide polymorphism surveys in European and African populations, we find evidence for extreme local rate variation spanning four orders in magnitude, in which 50% of all recombination events take place in less than 10% of the sequence. We demonstrate that recombination hotspots are a ubiquitous feature of the human genome, occurring on average every 200 kilobases or less, but recombination occurs preferentially outside genes.

The nature and causes of recombination rate variation in the human genome are little known. Genetic maps estimated from pedigree studies have revealed chromosome-wide and sex-specific variation in the rate of recombination (*1*, *2*) but only have resolution above megabase scales. Analyses of recombination break points and, more recently, cross-over events in sperm have demonstrated the presence of recombination hotspots in a small number of genomic locations; the human leukocyte antigen (HLA) region (*3*, *4*), the minisatellite MS32 (*5*), the pseudoautosomal region (*6*), and the β-globin gene (*7*). Hotspots are a feature described in yeast and some prokaryotes (*8*) but not documented in other eukaryotes such as flies and worms. However, recent observations of a block-like structure to patterns of human linkage disequilibrium (*9*–*11*) and correlations in homozygosity (*12*) have led to speculation that most or all human recombination occurs at hotspots (*9*, *13*). But, in fact, it is not known how widespread hotspots are in the human genome, neither is the magnitude of rate differences, nor the physical scales over which this occurs, known.

An understanding of the genomic landscape of human recombination rate variation would facilitate the efficient design and analysis of disease association studies and greatly improve inferences from polymorphism data about selection and human demographic history. Fine-scale recombination rate estimates would also provide a new route to understanding the molecular mechanisms underlying human recombination. Current approaches cannot provide this information: Pedigree studies do not have the required resolution, whereas sperm analyses can only detect recombination rate variation in males and are impracticable for studies on chromosomal scales. Here, we present and validate a coalescent-based method for estimating recombination rate variation at kilobase scales from large surveys of single-nucleotide polymorphism (SNP) variation. With the advent of genome-wide diversity studies, such as the HapMap (*14*), this will allow the construction of the first fine-scale genetic map in humans.

Patterns of genetic diversity and LD are shaped by many factors (*15*), mutation, recombination, selection, population demography, and genetic drift. Typically, they display substantial stochastic variation. Extracting the signal of recombination rate variation from such data presents a challenging statistical problem (*16*). Our approach, based on an approximation to the coalescent, is motivated by recent developments in computationally intensive population genetics inference methods (*17*–*19*). Informally, we extend the composite likelihood approach of Hudson (*20*) to allow different recombination rates between each pair of SNPs and adopt a Bayesian implementation in which the prior distribution encourages short-range smoothness in estimated recombination rates and avoids over-fitting (fig. S1 and table S1).

[1]Department of Statistics, University of Oxford, Oxford OX1 3TG, UK. [2]Wellcome Trust Sanger Institute, Hinxton, Cambridge CB10 1SA, UK.

*These authors contributed equally to this work.
†To whom correspondence should be addressed. E-mail: mcvean@stats.ox.ac.uk